# A Microscopic Telepathology System for Multiresolution Computer-Aided Diagnostics

Grigory Begelman, Michael Pechuk, Ehud Rivlin
Department of Computer Science, Technion – Israel Institute of Technology, Haifa, Israel
{gbeg,mpechuk,ehudr}@cs.technion.ac.il
Edmond Sabo, M.D.
Department of Pathology, Rhode Island Hospital and Brown School of Medicine, Providence, Rhode Island
esabo@lifespan.org

***Abstract*— The aim of the presented system is simplification and speedup of the daily pathological examination routine. The system combines telepathology with computer-aided diagnostics algorithms. To the best of our knowledge, this is the first approach proposing such a comprehensive method. Our system is designed to accumulate knowledge through a learning process during diagnostics. Our system targets image acquisition and interpretation stages. The image acquisition subsystem solves various problems related to microscopical slide digitization such as biomedical image registration, data representation, and processing. The interpretation subsystem is based on Gabor filter texture features as well as on color features. A support vector machine classifier together with a feature selection is used for computer-aided diagnostics. The system design allows easy adaptation to a wide range of microscopical pathology examinations. The system is easily deployed and scaled. It has a low support cost and can aggregate a wide range of existing hardware. The experimental validation of the system is based on a database of more than three thousand samples. During the experimental evaluation, the system exhibited successful interaction with a pathologist.**

***Index Terms*— computer-aided diagnostics, microscopical telepatology, multiresolution analysis**

## I. Introduction

Many different pathologies can be detected by microscopic examination of histological tissues. For example, prostate carcinoma, breast cancer, etc are be identified through such procedures. In this paper we describe a system aimed at facilitating the diagnosis of such diseases. We validate the system design and efficiency in the diagnosis of prostate carcinoma.

Prostate carcinoma is the second most common cause of cancer deaths among men in the United States. The diagnostics of prostate carcinoma involves pathology analysis of prostate tissue. Gleason grading [1] is the most widely used grading system for estimating the level of aggressiveness of the prostate carcinoma. The grading has five levels of severity, corresponding to five different architectural patterns formed by the prostate glands (see Fig. 1). The routine for pathology analysis of prostate tissue, widely accepted in hospitals, includes the following:

1) Obtaining a specimen from a patient.
2) Preparing the specimen (staining, sectioning, and mounting on glass slides).
3) Microscopic examination of the prepared specimen by a screener. At this stage, the screener locates and marks suspicious regions on the slides.
4) Microscopic examination of the marked regions by a pathologist. At this stage, the pathologist gives the final diagnosis.

The classical routine of pathology analysis of the prostate tissue has a number of shortcomings:

- The human factor may cause diagnostic inaccuracy.
- The heavy load on pathologists. A pathologist in a typical laboratory analyzes many slides per day.
- Interobserver disagreement [2], [3]. The Gleason grading system is subject to interobserver disagreement.The final diagnosis for the same specimen given by different pathologists may differ.
- Second opinion problem. For difficult cases, a second opinion is often necessary, requiring physical transfer of the slide. As a result, patients wait more time to get a conclusive diagnosis.

Systems with computer-aided diagnostics and telepathology capability will help to eliminate the shortcomings of the classical pathology routine. Some diagnostic tasks can already be reliably performed by computer. For example, a system for automated Pap smear screening [4] achieves similar or higher accuracy compared to the classical methods of examination. Several researches have investigated computer-aided diagnostics of prostate carcinoma, e.g., [5]–[7]. At the same time, advances in computer networking now provide the possibility of telepathology: distant diagnosis of specimens (e.g., [8]–[15]).

We present a system combining the advantages of computer-aided diagnostics, active learning algorithms, and telepathology. Our system addresses the problems of the classical routine. It automates detection of suspicious regions on the microscopic slides, assists pathologists in diagnostics, and, finally, provides an environment for distant collaborative diagnostics.

The paper is organized as follows. In Section II, the structure of the proposed system is explained. In Section III, the experimental result are presented. Finally, we conclude in Section IV.

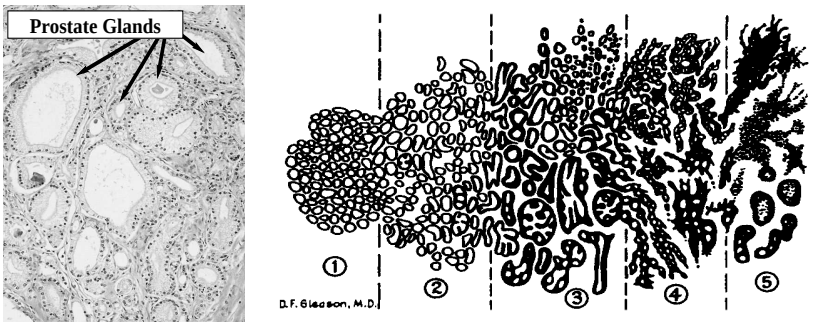


(a) (b)

Figure 1. Gleason grading of prostate carcinoma. Prostate glands (a) form patterns used for Gleason grading. Five Gleason grades of prostate cancer correspond to five patterns formed by prostate glands (b).

## II. System Structure

The structure of our system for computer-aided microscopic pathology diagnostics is presented in Fig. 2(a). Our system combines image acquisition and interpretation phases(see Fig. 2(b) and 2(c)). It targets the last two steps of the classical routine: microscopic examination of the prepared specimen by a screener and microscopic examination of the marked regions by a pathologist.

The system comprises the following components: a computer-aided diagnostics component, a slide scanner, and a telepathology interface. Below we describe these components in detail.

### *A. Computer-aided Diagnostics Component*

This component analyzes the scanned slide and generates hypotheses about optimal magnification for analysis and diagnosis of each slide region. The component uses an active learning algorithm for knowledge accumulation during primary learning. Feature selection algorithms are used to eliminate redundant and irrelevant features. During diagnostics the component refines obtained knowledge using the pathologists' feedback. In the following section we describe the implementation details of the component.

**Multiresolution Analysis** Traditionally, pathology analysis of tissues is performed under several magnification levels. Different characteristics of the examined tissues are revealed under various magnifications. For example, in Fig. 3(a) the morphology of prostate glands is observed under $\times 40$ magnification, while in Fig. 3(b) the structure of cells' nuclei is observed under $\times 100$ magnification. Our system allows multiresolution analysis via the telepathology interface (see section II-C). In addition, the system is designed to determine the optimal magnification levels for the slide regions. This is done by classifying the slide tiles into one of two categories: "suitable for analysis under $\times 40$ magnification" and "need better magnification". The classifications for initial training were provided by the expert pathologist. The following sections provide more details on feature extraction for the classifier and building the classifier.

**Feature Computation** The Gleason system is based on the architectural pattern of the glands of the prostate tumor. According to [7], [16], the architectural pattern of the prostate glands is well modeled by texture descriptors. Gabor filters are widely used in texture analysis applications [17], including texture classification, texture segmentation and image retrieval. The family of two-dimensional Gabor functions is defined as

$$G(x,y) = e^{-\frac{x'^2}{2\sigma_x^2}} e^{-\frac{y'^2}{2\sigma_y^2}} cos(\frac{2\pi x'^2}{\lambda} + \phi),$$

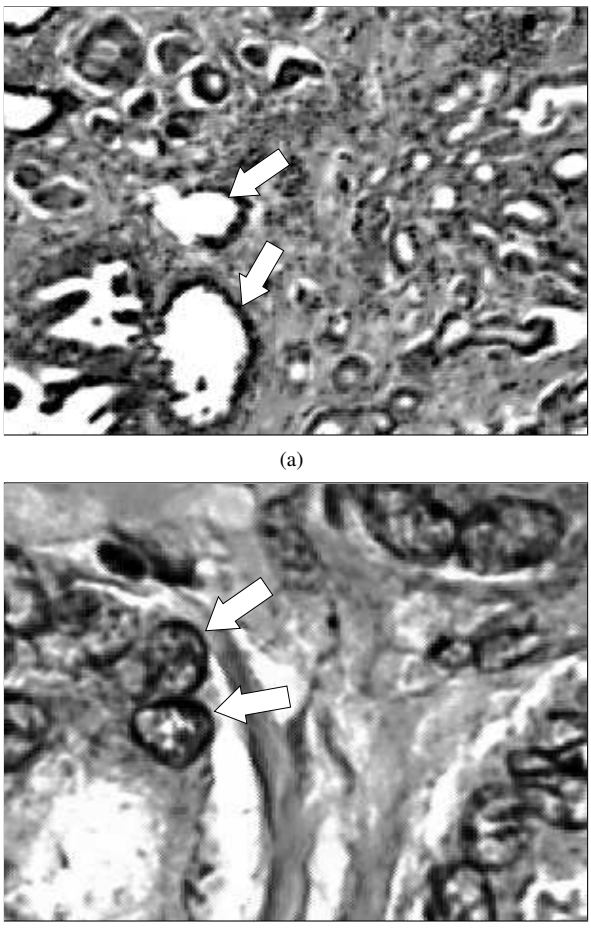

(a)

(b)

Figure 3. The characteristic objects of the prostate tissue captured under various magnifications. The characteristic objects are accented by white arrows. Prostate glands are observed under magnification $\times 40$ (a). Cell nuclei are observed under magnification $\times 100$ (b).

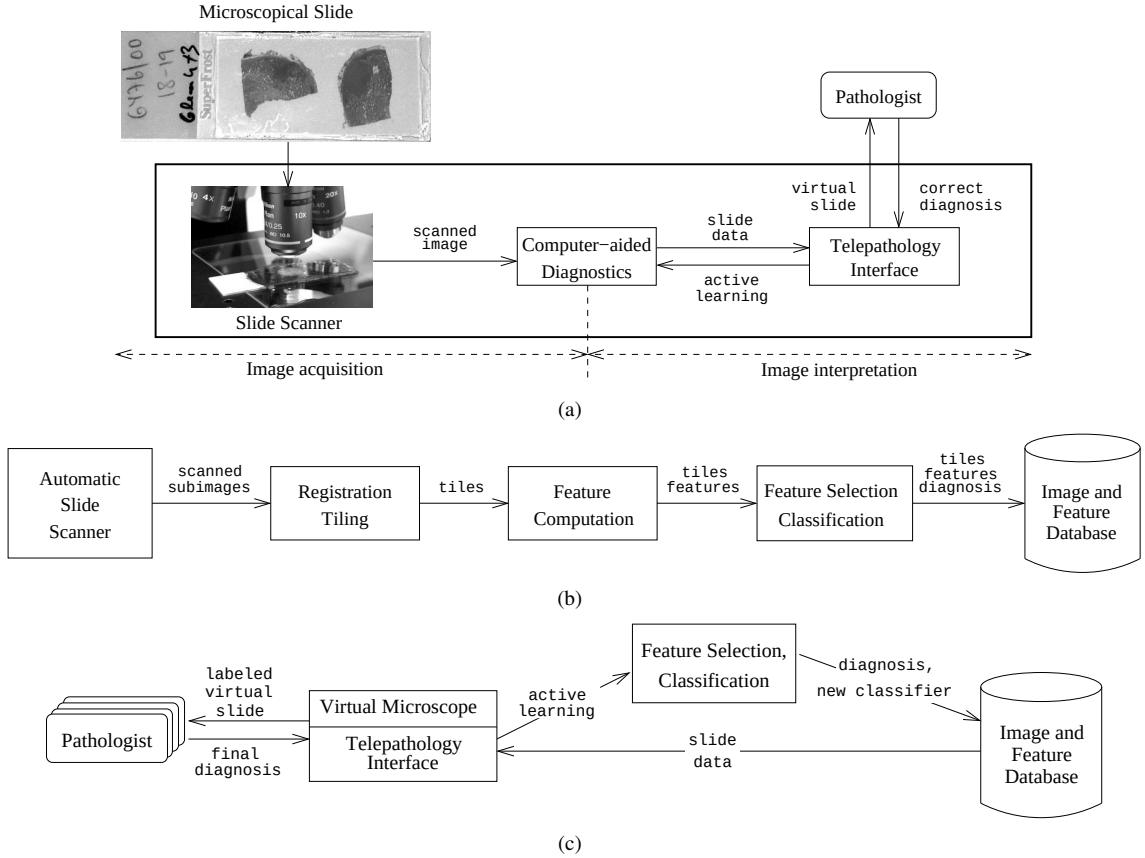


Figure 2. The main system components and their interactions. The arrows denote information and control flow. High-level system overview (a). Image acquisition scenario (b). Image interpretation scenario (c).

where

$$\begin{cases} x' = (x - m_x)cos(\gamma) - (y - m_y)sin(\gamma) \\ y' = (x - m_x)sin(\gamma) + (y - m_y)cos(\gamma) \end{cases}$$

- $\gamma$ specifies the orientation
- $\phi$ specifies the phase offset
- $(m_x, m_y)$ specify the center of the receptive field in image coordinates
- $(\sigma_x, \sigma_y)$ determines the size of the receptive field
- $\frac{1}{\lambda}$ is the preferred spatial frequency of $G$

In our experiments we used a bank of Gabor filters with six equidistant orientations and four spatial frequencies. The bank of Gabor filters is presented in Fig. 4. Mean and standard deviation of the response energies for each orientation and scale of a Gabor filter in the bank constitute texture features.

Prostate tissue subject to microscopic examination is stained by the histochemical dyes hematoxylin and eosin. Nuclei of cells are stained in various blue hues (basophilic stain) and surrounded by a pinkish background (eosinophilic stain). We used values from the 10-bin hue histogram as color features.

**Classification** For classification we used a Support Vector Machine (SVM) algorithm. Support vector machines, a supervised machine learning technique, have solid theoretical justification [18] and perform well in multiple areas of biological analysis (see the survey of SVM applications to biological problems in [19]). We built the SVM classifier, determined its optimal parameters and estimated the classifier performance using the method described in the next section.

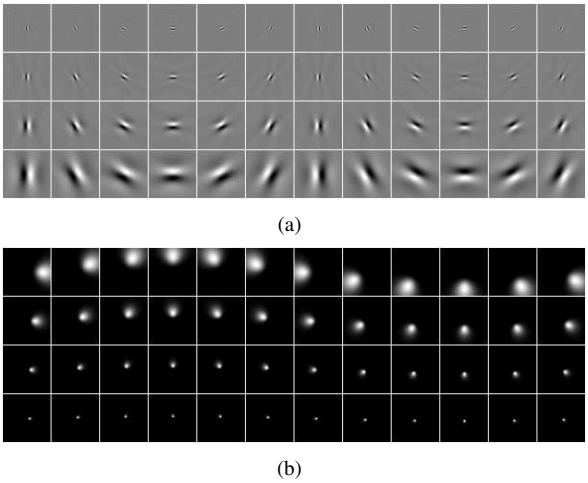

(a)

(b)

Figure 4. Bank of Gabor filters (six equidistant orientations and four spatial frequencies). Odd filters in the spatial domain (a) and filter bank in the frequency domain (b).

**Training-Validation Protocol** A frequently employed method to estimate the classifier's performance is to split the data into a training set and testing set. The training set is used to construct the classifier. The testing set is used to estimate the performance of the classifier on unseen

samples. There are several popular methods for dividing the data into training and validation sets. We choose the cross-validation method [20], which provides an accurate estimation for real-world problems [21].

The training protocol (see Fig. 5) delivers, given a training dataset, an estimate of $\hat{L}_A$ for the best achievable error of learning algorithm $A$. To this end, the training dataset $S$ is randomly permuted and partitioned into $N_{folds}$ subsets of equal size $S_1, \ldots, S_{N_{folds}}$. $N_{folds}$ training/testing datasets are constructed as follows: $S^i_{test} = S_i$ constitutes a testing partition and $S^i_{train} = S \backslash S_i$ constitutes a training partition ($i = 1 \ldots N_{folds}$). Then the classifier is constructed for the training partition, and its performance is evaluated on the testing partition. As the SVM classifier with an RBF kernel is a parametric classifier, the process of classifier construction for each testing partition involves optimization of the RBF kernel parameters to maximize the classifier performance. To achieve this, the testing partition is randomly divided into $N_{val}$ subsets of equal size, and $N_{val}$ training/validation partitions $V^j_{train}, V^j_{test}$ are constructed in a similar manner ($j = 1 \ldots N_{val}$). Then, for each feasible hyper-parameter vectors $\theta \in \Theta$, a classifier is constructed on the training partition $V^j_{train}$ and the performance $\hat{L}_A(i, j, \theta)$ is evaluated on the corresponding testing partition $V^j_{test}$. Then the error $\hat{L}^{med}_A(i, \theta)$ is computed as the median of $\hat{L}_A(i, j, \theta)$ and, finally, the best hyper-parameters are selected $\theta^*_i = argmin_\theta \hat{L}^{med}_A(i, \theta)$. The hyper-parameters $\theta^*$ are used to construct the classifier for the training set $S^i_{train}$. Thereafter, the classification error $\hat{L}_A(i)$ is evaluated on $S^i_{test}$. Eventually, the classification error is calculated as mean of all classification errors $\hat{L}_A(i)$, $i = 1 \ldots N_{folds}$.

**Feature Selection** Some features may be irrelevant or redundant. Large amounts of irrelevant features affect learning algorithms at three levels [22]. First, most learning problems do not scale well with the growth of irrelevant features. Second, classification accuracy degrades for a given training set size. The third aspect concerns the run time of the learning algorithm. Following Wolf et al. [22], we select feature subset providing the best cluster arrangement of the data points in the feature space. The selected subset is fed to the classifier.

**Primary Learning** Usually, in order to train a classifier, a significant representative set of labeled samples is required. Therefore, a pathologist should label a significant number of sample regions. However, in most cases the total area occupied by irrelevant and normal regions is much larger compared to the area taken up by suspect regions. Thus, the probability of running across a diseased region is low. A pathologist may screen hundreds of images without coming across an area that requires special investigation. In order to boost the primary learning, we use the active learning algorithm described in [23]. Only images whose grading improve the expected performance of the SVM classifier are provided to a pathologist. After each iteration a new SVM classifier is built, according to the protocol described in Fig. 5, and the sample selection continues.

**Require:** 1) A labeled dataset $S = \{(x_i, y_i)\}_{i=1}^m$
2) A learning algorithm $A(\theta)$
3) A set $\Theta$ of feasible hyper-parameter vectors
4) $N_{folds}$ = number of folds
5) $N_v$ = number of validation folds

**Ensure:** An estimate $\hat{L}_A$ for the best achievable error of the learning algorithm $A$ trained on a set of size $|S|(1 - 1/N_{folds})$.

1: Randomly permute and partition $S$ into $N_{folds}$ subsets of equal size; denote these subsets by $S_1, \ldots, S_{N_{folds}}$ these subsets
2: Construct $N_{folds}$ training/test partitions $(S^i_{train}, S^i_{test})_{i=1}^{N_{folds}}$ such that $S^i_{train} = S \backslash S_i$ and $S^i_{test} = S_i$
3: **for** $1 \leq i \leq N_{folds}$ **do**
4:  **for all** $\theta \in \Theta$ **do**
5:  Randomly permute and partition $S^i_{train}$ into $N_{val}$ subsets of equal size; denote these subsets by $V^i_1, \ldots, V^i_{N_{val}}$ these subsets.
6:  Construct $N_{val}$ train/test partitions $(V^{i,j}_{train}, V^{i,j}_{test})_{j=1}^{N_v al}$ such that $V^{i,j}_{train} = S^i_{train} \backslash V^i_j$ and $V^{i,j}_{test} = V^i_j$.
7:  **for** $1 \leq j \leq N_{val}$ **do**
8:  Compute $\hat{L}_A(i, j, \theta) = \hat{L}_A(V^{i,j}_{test} | \theta, V^{i,j}_{train})$
9:  **end for**
10:  Compute the median $\hat{L}^{med}_A(i, \theta)$ of $\{\hat{L}_A(i, j, \theta)\}_{j=1}^{N_v al}$
11:  **end for**
12:  Let $\theta^*_i = argmin_\theta \hat{L}^{med}_A(i, \theta)$
13:  Compute $\hat{L}_A(i) = \hat{L}_A(S^i_{test} | \theta^*_i, S^i_{train})$.
14: **end for**
15: **return** $\frac{1}{N_{folds}} \sum_i \hat{L}_A(i)$

Figure 5. Experiment protocol for estimation of the classification error.

### *B. Slide Scanner*

The slide scanner component digitizes an analyzed slide. The digitization includes capturing sub-images (adjacent regions of slides), registering them, and, finally, slide tiling. The following section describes the implementation details of the slide scanner component.

**Sub-image capturing** Time spent for sub-image capturing is the bottleneck of slide digitizing. The motion of the mechanical microscope stage is the most time consuming part of sub-image capturing. In order to minimize the overall time of microscope stage travel, we use the boustrophedon scanning route [24]. The scan direction of consecutive scan bands are alternated.

The white point of the captured images differs from the computer monitor's white point. In addition, each pixel has a different white point. This difference is introduced by the microscope lamp, the optical path, and also the digital camera. Since the parameters of the microscope lamp, the microscope optical path, and the camera do not change during the slide digitization, we can assume that each pixel has an individual independent color aberration model. The color models for each pixel are computed from the captured images of the empty slide regions

once per hardware adjustment. To this end, we take the median of pixel values in XYZ color space and adjust the white point to match the D50 white point ($X = 0.9642$, $Y = 1.000$, $Z = 0.8249$) – the white point of a correctly calibrated monitor (see the example of color correction in Fig. 6).

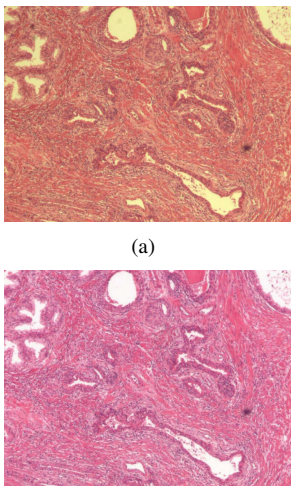

(a)

(b)

Figure 6. Example of color correction for a captured image. Before color correction (a): white does not correspond to the white color of a correctly calibrated monitor. After color correction(b): white corresponds to the white color of a correctly calibrated monitor.

**Sub-image registration** The mechanical precision of the motorized microscope stage is limited. Therefore, image processing techniques should be used to register the adjacent sub-images. We register each image to its right and bottom neighboring sub-images. Sufficient overlapping of the registered sub-images is the necessary condition for registration. We use a phase correlation technique for image registration due to its reliable work on relatively small overlapping regions and good time performance.

Due to the properties of the microscopic stage moving mechanism and microscope optics, the transformation between two adjacent sub-images is limited to translation. We successfully verified this hypothesis experimentally. If $f_2(x, y)$ is a translated replica of $f_1(x, y)$ with translation $(x_0, y_0)$, then $f_2(x, y) = f_1(x - x_0, y - y_0)$. According to the Fourier translation property, the Fourier transforms of $f_1(x, y)$ and $f_2(x, y)$ are related by

$$F_2(\xi, \eta) = e^{-2\pi i(\xi x_0 + \eta y_0)} F_1(\xi, \eta).$$

The cross-power spectrum of the two images $f_1$ and $f_2$ is defined as:

$$\frac{F_1(\xi, \eta) F_2^*(\xi, \eta)}{|F_1(\xi, \eta) F_2(\xi, \eta)|} = e^{-2\pi i(\xi x_0 + \eta y_0)}$$

The inverse Fourier transform of the cross-power spectrum results in an impulse function

$$\mathcal{F}^{-1}\{e^{-2\pi i(\xi x_0 + \eta y_0)}\} = \delta(x + x_0, y + y_0)$$

Ideally, the peak value of the impulse function should be equal to 1.0. However, due to the presence of noise and dissimilar parts in the sub-images, the delta function degrades. Therefore, the translation parameters are estimated by

$$(x_0, y_0) = \arg\max\{\mathcal{F}^{-1}\{e^{-2\pi i(\xi x_0 + \eta y_0)}\}\}.$$

We follow the method described in Keller et al. [25] to obtain sub-pixel registration accuracy.

To achieve better time performance of the registration we adopt a multiresolution approach. First, a coarse registration is performed on images scaled down by 0.2. Second, the sub-pixel registration accuracy is achieved by registering only the intersecting parts of the images.

**Require:** 1) A set of captured sub-images $I_{ij}$.
2) Transformations $T_{i_1 j_1} - T_{i_2 j_2}$ between adjacent sub-images $I_{i_1 j_1}$ and $I_{i_2 j_2}$
**Ensure:** Tiles: ideally aligned non-overlapping images covering the whole slide area.
1: Detect connected components on the scanned slide
2: **for all** connected components **do**
3: Calculate global transform for all captured sub-images relating to the origin of the central image of the connected component.
4: Calculate the coordinates of the tiles relating to the origin of the central image of the connected component.
5: Build the tiles from the corresponding images
6: **end for**

Figure 7. Algorithm of tiles construction from the captured sub-images.

**Slide tiling** The resulting size of microscopic slides digitized under $\times 100$ magnification is in tens of giga-pixel range. Such a volume of data causes technical difficulties for storing and accessing the images. The digitized slides are accessed via a computer network, so to make the data transfer efficient we divide the whole slide into relatively small tiles. The tiles are ideally aligned non-overlapping images covering the whole slide area.

Due to the large volume of the resulting digitized slide it is impractical to construct the whole slide and then to divide it into tiles. Instead, we construct the tiles directly from the captured sub-images and the transformation between the adjacent sub-images. The tiles construction algorithm is presented in Fig.7.

Each slide may include several disconnected tissue parts. This problem is addressed by detecting connected components using the transformations between adjacent sub-images. To accomplish this we build an undirected graph representing registration results. The vertices of the graph are the origins of the sub-images. The edges of the graph connect vertices corresponding to adjacent sub-images, if the registration between these sub-images was successful. This graph may contain several connected components corresponding to disconnected fragments of the tissue. Once we identify the connected components, tiles are constructed for each component separately.

We take the origin of the central image of each component as a global origin. Then we calculate the global

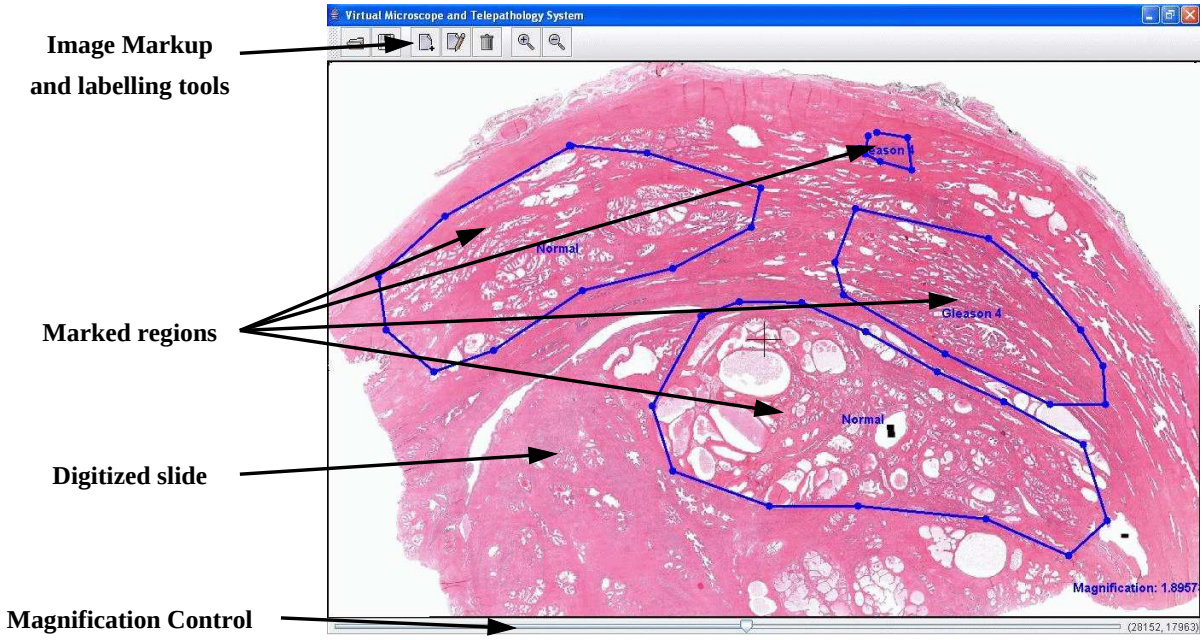


Figure 9. Application screen-shot. The main controls (image markup, labeling tools and magnification control), a digitized slide, and the regions marked on the slide are denoted by arrows.

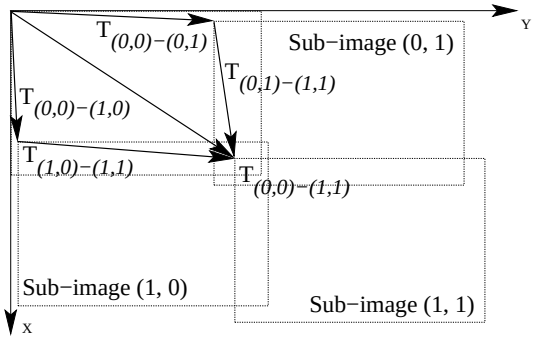


(a)

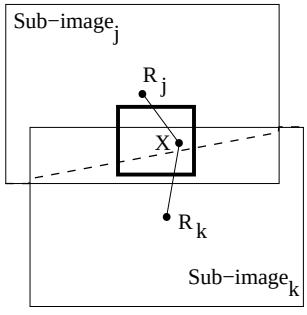


(b)

Figure 8. (a) Image registration. Images are captured with intersection. Sub-image (0,0) denotes the central image. $T_{i-j}$ is the transformation between the origins of sub-images $I$ and $J$. (b) Tile construction. The constructed tile is denoted by the bold line. $R_j$ and $R_k$ are the centers of the sub-images. $X$ is a tile pixel. The dashed line is the border between the Voronoi cells corresponding to $R_j$, $R_k$.

transform of each sub-image of this connected component in a breadth-first search (BFS) order starting from a central sub-image. For some sub-images several variants of the global transform may be calculated. For example, the global transform for sub-image $(1,1)$ in Fig. 8(a)) may be calculated as

$$T^1_{(0,0)-(1,1)} = T_{(1,0)-(1,1)} T_{(0,0)-(1,0)}$$
$$T^2_{(0,0)-(1,1)} = T_{(0,1)-(1,1)} T_{(0,0)-(0,1)}.$$

In such cases, the resulting global transform for this sub-image is taken as average:

$$T_{(0,0)-(1,1)} = \frac{T^1_{(0,0)-(1,1)} + T^2_{(0,0)-(1,1)}}{2}$$

After calculating the global transform for each sub-image, we build tiles of the connected component. First, the tiles are positioned to cover the whole connected component, and the tile coordinates are calculated. Then, we build Voronoi diagram on the centers $R_i$ of the sub-images and use it for efficient calculation of the nearest sub-image for the tile pixels (see Fig. 8(b)).

### C. Telepathology Interface

The telepathology interface provides a convenient multi-user environment for interaction with our system. To enable fast system adoption by pathologists, the interface was build to resemble the microscopic environment (see the screenshot of the telepathology interface application in Fig. 9). To this end, a pathologist may browse digital slides using the client software by fast panning (simulates movement of the microscope stage), zooming in/out to/from arbitrary selected regions up to a predefined resolution (simulates magnification changes).

In addition, to provide pathologists a means of communicating with the system and with each other, the interface allows image labeling by selecting a digital slide region and assigning a diagnosis and an arbitrary comment. All interesting/suspicious regions detected by the CAD

TABLE I.
EXPERIMENTAL DATABASE CONTENTS.

| | $\times 40$ magnification | $\times 100$ magnification |
|---|---|---|
| Normal or Non-Relevant | 863 | 2304 |
| Gleason 3 | 59 | 329 |
| Gleason 4 | 10 | 37 |
| Gleason 5 | 0 | 139 |
| Need Better Magnification | 111 | NA |

TABLE II.
CLASSIFICATION ACCURACY ESTIMATED BY FIVE-FOLD CROSS-VALIDATION METHOD.

| Classification categories | Accuracy |
|---|---|
| $\times 40$ magnification vs. $\times 100$ magnification | 93% |
| "Normal or Non Relevant" vs. "Attention Required" under $\times 40$ magnification | 95% |
| "Low Gleason" (i.e., Gleason 3) vs. "High Gleason" under $\times 40$ magnification | 98% |
| "Low Gleason" (i.e., Gleason 3) vs. "High Gleason" (i.e., Gleason 4 and Gleason 5) under $\times 100$ | 88% |

component are presented at relevant magnification in order to speedup the diagnosis process. Comments and labeling are stored in a database along with the slide and can be viewed by all authorized users. Moreover, the final diagnosis is provided to the CAD system in order to improve classification results. The features of the user interface allow convenient communication and discussion of difficult cases within a wide audience of pathologists and provide the option for a second opinion in timely manner and without physically having to transfer the slide.

The telepathology interface was built using the client-server architecture. Since the Internet is a common and affordable data transfer infrastructure, we chose it to be the communication layer between the client and the server. The implemented interface uses the Secure Socket Layer provided by a standard library to ensure encrypted communication between the client and the server. The server side is responsible for storing the digitized slides database. The database consists of

- the digitized slides tiles
- the regions, created by pathologists using the slide labeling tool and by the system as a result of computer-aided diagnostics
- the slides' meta-information

The server side is based on open-source free domain software. We selected MySQL 5.0 for the database engine. All communication between the user interface application and the database is implemented over the HTTP protocol, and an Apache HTTP server handles the HTTP requests. Both MySQL and the Apache HTTP server are scalable and exist in a wide range of platforms. This makes our system easily deployable and scalable. The system has a low support cost and can aggregate wide range of existing hardware.

The client side application is written in Java to provide high compatibility with a wide range of platforms. The interface provides the possibility of a low magnification slide overview and a high magnification study of the possible diagnostic details. To ensure high responsiveness of the telepathology interface, the digital slides are compressed after scanning and tiling.

At the first step of slide compression algorithm, a Gaussian pyramid of the slide image is built for bandwidth-efficient presentation of the slide at different magnification levels. Then each level of the pyramid is divided into small sub-images of dimension $256 \times 256$ pixels in size. These sub-images are stored in the database after compression using a JPEG compression algorithm [26].

This method allows that only data relevant to the current resolution and position to be transferred to the client. This is an important feature of the system, because the requirement of storing (and potentially presenting) the whole digitized slide leads to huge data volumes. For example, the $\times 100$ scanning magnification implies a resolution of approximately $100000 \times 500000$ pixels or approximately 10Gb raw data per slide.

To utilize all available bandwidth, the client application is designed to transfer simultaneously a number of these sub-images. The sub-images neighboring to currently viewed region are downloaded in background. The combination of the image storing and caching techniques makes the scheme low bandwidth consuming and responsive.

## III. EXPERIMENTAL RESULTS

The hardware part of our system consists of a Nikon Eclipse E600 microscope equipped with a motorized stage, a Point Grey CCD camera and a Xeon 2.4GHz based computer. We experimented with histological slides of prostate tissue samples, sectioned into five micron thick slices and stained by the histochemical dyes hematoxylin and eosin. The slides contained all types of tissue, from normal tissue to Gleason 5. The tile dimensions were $1024 \times 1024$ pixels. To establish ground truth and to train the computer-aided diagnostics component, a number of tiles were graded by an expert pathologist according to the Gleason method. The tiles were classified as: "Normal or not relevant", "Gleason 3", "Gleason 4", "Gleason 5", and "Need better magnification". A tile was classified as "Need better magnification" if the pathologist had

difficulties in grading the tile under $\times 40$ magnification. The ground truth for the optimal magnification level and diagnosis was provided by an expert pathologist for $3852$ tiles (see Table I).

The classifiers ensuring the lowest classification error were built using the protocol described above (see Fig. 5). The learning algorithm $A$ is SVM, the set $\Theta$ of feasible hyper-parameters is the set of radial-based function kernel parameters, sampled by the grid search method. Finally, $N_{folds} = 5$, and $N_v = 5$.

The classification results are presented in Table II. The accuracy of correct magnification detection allows the pathologist to rely on the system for choosing the correct resolution for diagnosis verification. The classification accuracy between different grades of cancer and normal tissue allows the system to assist pathologists in diagnostics.

The Receiver Operating Characteristic (ROC) curve of the classifiers are presented in Fig. 10. From the ROC curve for "Normal Tissue" vs. "Attention Required" (Gleason 3, Gleason 4, Gleason 5) we see that it is possible to achieve a high true positive rate while keeping the false positive rate relatively low.

## IV. Conclusions

In this paper we presented a system for computer-aided multiresolution microscopic pathology diagnostics. To the best of our knowledge, this is the first approach combining the principle of telepathology with computer-aided diagnostics algorithms. The telepathology interface makes a second opinion available fast, without the actual need to physically transfer the slide. The system design implies that a diagnosis is approved by an expert pathologist in accordance with the hospital's standard procedure. Therefore the system can be gradually introduced into pathology departments. Consequently, the load placed on pathologists should be noticeably reduced due to the automatization of the routine work. This, in turn should diminish the risk of errors and interobserver diagnostic disagreement. The software implementation of the system is based on platform-independent and scalable software. The system is easily deployed and scalable. The system has a low support cost and could aggregate a wide range of existing hardware. The system design and efficiency was validated on diagnostics of prostate carcinoma. The successful experimental validation of the system is based on a database of more than three thousand samples. During the experimental evaluation, the system exhibited successful interaction with a pathologist and diagnostics speedup.

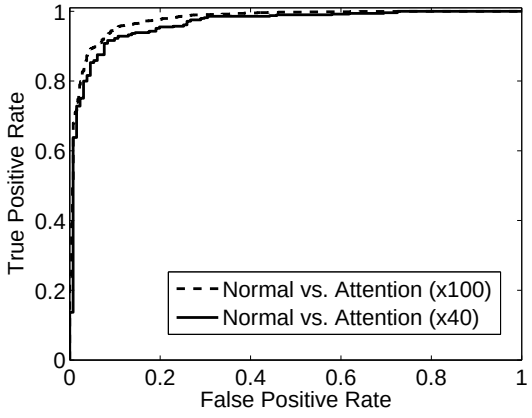


(a)

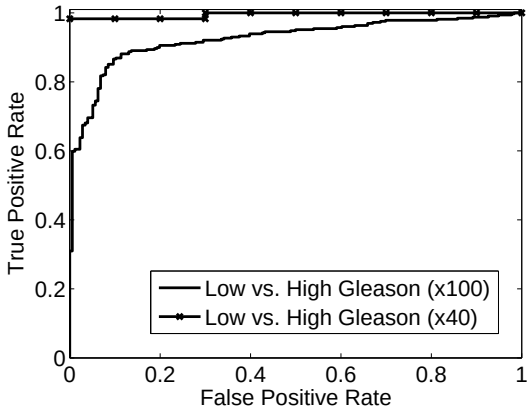


(b)

Figure 10. Receiver Operating Characteristic curves of the classifiers. (a) "Normal Tissue" vs. "Attention Required". The area under the ROC curve for magnification $\times 40$ is $0.96$ and for magnification $\times 100$ is $0.98$. (b) "Low Gleason" vs. "High Gleason". The area under the ROC curve for magnification $\times 40$ is $0.99$ and for magnification $\times 100$ is $0.93$.

## References

[1] D. G. Bostwick and J. N. Eble, *Urologic Surgical Pathology*. New York, NY: Mosby - Year Book Inc., 1997.

[2] A. Taille, A. Viellefond, N. Berger, and et al., "Evaluation of the interobserver reproducibility of gleason grading of prostatic adenocarcinoma using tissue microarrays," *Human Pathology*, vol. 34, pp. 444–449, 2003.

[3] W. Allsbrook, K. Mangold, M. Johnson, R. Lane, C. Lane, and J. Epstein, "Interobserver reproducibility of gleason grading of prostatic carcinoma: general pathologist," *Human Pathology*, vol. 32, pp. 81–88, 2001.

[4] C. Sturgis, C. Isoe, N. McNeal, G. Yu, and D. DeFrias, "Papnet computer-aided rescreening for detection of benign and malignant glandular elements in cervicovaginal smears: A review of 61 cases," *Diagnostic Cytopathology*, vol. 18, no. 4, pp. 307–311, 1998.

[5] A. Wetzel, R. Crowley, S. Kim, R. Dawson, L. Zheng, Y. Joo, Y. Yag, J. Gilbertson, C. Gadd, D. Deerfield, and M. Becich, "Evaluation of prostate tumor grades by content-based image retrieval." in *SPIE Workshop: Advances in Computer-Assisted Recognition*, vol. 3854, 1999, pp. 244–252.

[6] Y. Smith, G. Zajicek, M.Werman, and G. P. Y. Sherman, "Similarity measurement method for the classification of architecturally differentiated images." *Computers and Biomedical Research*, vol. 31, no. 1, pp. 1–12, 1999.

[7] K. Jafari-Khouzani and H. Soltanian-Zadeh, "Multiwavelet grading of pathological images of prostate," in *IEEE Transactions on Biomedical Engineering*, vol. 50, 2003, pp. 697–709.

[8] G. Begelman, M. Lifshits, and E. Rivlin, "Map-based microscope positioning," in *British Machine Vision Con-*

*ference*, 2004.

[9] A. Sussman, A. Demarzo, A. Afework, F. Bustamante, H. Tsang, M. Silberman, M. D. Beynon, and R. Ferreira, "Digital dynamic telepathology – the virtual microscope," in *American Medical Informatics Association Fall Symposium*, 1998.

[10] U. Catalyurek, M. D. Beynon, T. C. C. Kurc, A. Sussman, and J. Saltz, "The virtual microscope," *IEEE Transactions on Information Technology in Biomedicine*, vol. 7, pp. 230–248, 2003.

[11] D. Comaniciu, W. Chen, P. Meer, and D. Foran, "Multiuser workspaces for remote microscopy in telepathology," in *Proceedings of IEEE Computer-Based Medical Systems*, vol. 2, 1999, pp. 150–155.

[12] S. Olsson and C. Busch, "A national telepathology trial in sweden: Feasibility and assessment," *Archives d'Anatomie et de Cytologie Pathologiques*, vol. 43, p. 234241, 1995.

[13] J. Z. Wang, J. Nguyen, K.-K. Lo, C. Law, and D. Regula, "Multiresolution browsing of pathology images using wavelets," in *American Medical Informatics Associationl Symposium*, 1999, p. 340344.

[14] M. Weinstein and J. I. Epstein, "Telepathology diagnosis of prostate needle biopsies," *Human Pathology*, vol. 28, no. 1, pp. 22–29, 1997.

[15] R. S. Weinstein, A. Bhattacharyya, A. R. Graham, and J. R. Davis, "Telepathology: A ten-year progress report," *Human Pathology*, vol. 28, no. 1, pp. 1–7, 1997.

[16] R. Stotzka, R. Manner, P. H. Bartels, and D. Thompson, "A hybrid neural and statistical classifier system for histopathologic grading of prostate lesions," *Analytical Quantitative Cytology and Histology*, vol. 17, no. 3, pp. 204–218, 1995.

[17] J. Daugman, "Complete discrete 2-d gabor transforms by neural networks for image analysis and compression," *Acoustics, Speech, and Signal Processing, IEEE Transactions on*, vol. 36, no. 7, pp. 1169–1179, 1988.

[18] V. Vapnik, *Statistical Learning Theory*. John Willey and Sons, Inc., 1998.

[19] W. Noble, "Support vector machine applications in computational biology," *Kernel Methods in Computational Biology*, pp. 71–92, 2004.

[20] E. Alpaydin, *Introduction to Machine Learning*. The MIT Press, 2004.

[21] R. Kohavi, "A study of cross-validation and bootstrap for accuracy estimation and model selection," in *IJCAI*, 1995, pp. 1137–1145.

[22] L. Wolf and A. Shashua, "Feature selection for unsupervised and supervised inference: the emergence of sparsity in a weighted-based approach." in *International Conference on Computer Vision*, 2003, pp. 378–384.

[23] S. Tong and E. Chang, "Support vector machine active learning for image retrieval," in *ACM International Conference on Multimedia*, 2001, pp. 107–118.

[24] D. Mark, "Neighbor-based properties of some orderings of two-dimensional space." *Geographical Analysis*, vol. 22, pp. 145–147, 1990.

[25] Y. Keller and A. Averbuch, "Fft based image registration," in *IEEE International Conference on Acoustics, Speech, and Signal Processing*, 2002.

[26] W. B. Pennebaker and J. L. Mitchell, *JPEG Still Image Data Compression Standard*. Norwell, MA, USA: Kluwer Academic Publishers, 1992.

**Grigory Begelman** received the B.Sc and M.Sc degrees in mathematics and physics from the Moscow Institute of Physics and Technology, Russia. Currently, he is a Ph.D student in the Computer Science Department at the Technion, Israel Institute of Technology. His current research interests are in computer-aided diagnostics, hyper-spectral microscopy, blind source separation, processing and analysis of microscopic images.

**Michael Pechuk** received the B.Sc degree in computer science from Haifa University, Israel. Currently he is an M.Sc student in the Computer Science Department at the Technion, Israel Institute of Technology. His current research interests are in machine vision and function-based recognition.

**Prof. Ehud Rivlin** received the B.Sc and M.Sc degrees in computer science and the MBA degree from the Hebrew University in Jerusalem, Israel and the Ph.D from the University of Maryland, USA. Currently, he is an associate professor in the Computer Science Department at the Technion, Israel Institute of Technology. His current research interests are in machine vision and robot navigation.

**Dr. Edmond Sabo** is a Research Associate at Rhode Island Hospital/Lifespan, in the Department of Pathology as well as an Assistant Professor of Pathology at Brown Medical School. He came to Rhode Island in 2004 from Israel where he worked as Director of Surgical Pathology Unit at Carmel Medical Center in Haifa. Dr. Sabo received his M.D. degree from University of Medicine and Pharmacy in Iasi, Romania and completed his residency in Pathology in Israel. His research subspecialty includes analysis of microscopical patterns in tumor tissues using chaos and fractal theories, computerized morphometry, Biostatistics and Artificial Intelligence.